Aggregated System Frequency Response Model Considering Load Dynamics for Future Power Systems

Xianchao Liu, Guoqing Li, Tao Huang, *Senior Member*, *IEEE*, Tao Jiang, *Senior Member*, *IEEE*, Soheil Saadatmandi, *Graduate Student Member*, *IEEE*, and Gianfranco Chicco, *Fellow*, *IEEE*

***Abstract*—Future power systems will be characterized by low levels of inertia and limited frequency regulation capacity due to the widespread use of renewable energy sources. Furthermore, the response of different types of loads to system disturbances significantly affects the frequency dynamics. To address these issues, this paper proposes an aggregated system frequency response model considering load dynamics. Initially, a dynamic model of different loads is established, followed by the derivation of a small-signal load model that affects the active power imbalance of the system. The active power variations of loads are categorized into three components: load voltage dynamics, load frequency dynamics, and load inertia contribution. These components are incorporated into the system frequency response model, which accounts for load active power dynamics. The final output is an aggregated reduced-order system frequency response model, where the aggregation is primarily weighted by the primary frequency regulation capability of the load, load capacity, and rotor kinetic energy. Finally, the accuracy and effectiveness of the proposed model are validated using the WECC 9-bus test system with power electronic sources, and the influence of load parameters on the frequency stability indicators is analyzed.**

***Index Terms*—Power system, inertia, frequency response, frequency regulation, load dynamics, small-signal model.**

I. Introduction

FREQUENCY stability refers to the ability of the power system to maintain its frequency within an acceptable range when there is a power imbalance between generation and load [1], [2]. The frequency stability of a power system mainly depends on the inertia of power sources and primary frequency reserves [3]. However, renewable energy sources (RESs) and power electronic devices with grid-following control do not participate in the frequency coupling process of the system, resulting in almost no inertial response and primary frequency regulation capability. This poses significant challenges to the frequency stability of future power systems with deep penetration of RESs and high proportion of power electronic devices.

Simultaneously, the proportion of dynamic components on the load side is increasing [4], [5]. For instance, the UK power system load side contributes 20% of the system inertia [6], indicating that the impact of diversified loads (particularly induction motors (IMs)) on system frequency cannot be ignored. Therefore, it is crucial to establish a frequency response model for diversified loads to accurately reveal their coupling mechanisms in the system frequency response (SFR).

The SFR model is commonly used to describe the frequency characteristics of the center of inertia in bulk power systems. The SFR model retains the rotor motion equations and simplifies the prime mover governor to a first-order transfer function, resulting in a simplified second-order SFR model [7]. In [8] and [9], an aggregated simplified second-order SFR model and analytical techniques are proposed based on the methodology in [7]. However, given the high robustness of future power systems, these methods treat the load frequency regulation effect as part of a constant system damping factor, which is only applicable to traditional power systems with a deep penetration of synchronous generators. Therefore, additional validation of the accuracy of the SFR model for emerging power systems is required.

In recent years, many efforts have been dedicated to analyzing the impact of loads on SFR models. In [10], loads are generally categorized into static and dynamic types. The well-known ZIP model (i.e., constant impedance (CI), constant current, constant power (CP)) represents the mechanism of static loads. CP loads do not have a frequency response in the context of frequency-active power problems [11]. However, for voltage-sensitive loads prevalent in actual power systems, active power imbalances alter the voltage magnitude and active power of CI loads through the power network, ultimately affecting the system frequency [12]. In [13], the frequency support role of voltage-sensitive loads under different voltage sag conditions is analyzed using time-

Manuscript received: October 31, 2024; revised: February 19, 2025; accepted: April 23, 2025. Date of CrossCheck: April 23, 2025. Date of online publication: May 23, 2025.

This work was supported in part by National Natural Science Foundation of China-State Grid Joint Fund for Smart Grid (No. U23B20131) and National Natural Science Foundation of China (No. 52377083).

X. Liu, G. Li, and T. Jiang are with the Department of Electrical Engineering, Northeast Electric Power University, Jilin, China (e-mail: 1202000005@neepu.edu.cn; lgq@neepu.edu.cn; tjiang@neepu.edu.cn).

T. Huang (corresponding author), S. Saadatmandi, and G. Chicco are with the Department of Energy, Polytechnic University of Turin, Turin, Italy (e-mail: tao.huang@polito.it; soheil.saadatmandi@polito.it; gianfranco.chicco@polito.it).

DOI: 10.35833/MPCE.2024.001177

domain simulations. In [14], the static sensitivity method is used to analyze the effect of generator voltage on voltage-sensitive loads. However, this method only captures the coupling mechanism between power system stabilizers and the active power of loads. Moreover, previous studies do not provide sufficient analysis of the relationship between active power disturbances and the extent of voltage sags affecting loads. Therefore, a more comprehensive investigation into the interactive influence among system disturbances, voltage-sensitive loads, and frequency is required for further research.

Dynamic loads such as IMs significantly impact the frequency response of power systems. In [15], the influence of IMs on the frequency response model of the system can be summarized in the primary frequency modulation effect of a constant damping factor. In [16], the IM contribution is extended into a proportional-differential form of the SFR model, where the differential term inhibits the rate of change of frequency (RoCoF), and the proportional term alters the frequency nadir. Additionally, in [17], a first-order small-signal linearization model of IMs is developed, revealing that the IM response lacks a derivative term, and the asynchronous inertia of IMs only affects the frequency nadir of the system. Previous research has disclosed that IMs can contribute to the system inertia because the rotor speed of IMs is related to the system frequency [18], [19]. The inertia contribution provided by dynamic loads can be obtained using the anticipated disturbance identification algorithm designed in other studies [20], [21].

The composite load model (CLM) developed by the Western Electricity Coordinating Council (WECC) incorporates both static and dynamic components, with a detailed derivation provided in [22]. In contrast, a data-driven generic load dynamic model is introduced in [23], which has been verified primarily for voltage stability. However, its frequency response characteristics in relevant applications still require further clarification.

Overall, the critical research gaps can be categorized into three key areas. ① Studies on dynamic active power response modeling and classification development for composite load types need further extensions to better represent the impact of aggregated loads. ② The influence of different load characteristics on system frequency requires rigorous theoretical investigation, particularly in developing analytical SFR models that incorporate load dynamics. ③ A systematic investigation is needed to quantitatively assess the impact of various load parameters on frequency stability in future low-inertia power systems.

To bridge the research gaps mentioned above, this paper establishes an aggregated SFR model considering load dynamics to clarify and analyze the impact of different types of loads on the SFR.

The main contributions of this paper are as follows.

1) A classification method for active power variations of composite load. Unlike existing studies that primarily focus on individual load characteristics [17], this work establishes a small-signal linearization model for the active power variations of composite load. The active power variations of composite load can be systematically categorized into three components: load voltage dynamics, load frequency dynamics, and load inertia contribution. This tripartite classification allows for more precise quantification of load impacts on the SFR.

2) Development of an aggregated SFR model considering load dynamics. The voltage variation of composite loads is derived through a systematic quantification of the sensitivity column vector of load voltage magnitude to active power variation, which explicitly characterizes the coupling between load voltage and active power disturbances. Subsequently, three active power variations of composite loads are systematically integrated into the conventional SFR model. Building upon this foundation, the proposed model is developed through capacity-weighted aggregation of all power sources and loads, which significantly extends the conventional SFR model proposed in [9].

3) Comprehensive analysis of load parameter impacts on system frequency stability. Building upon the proposed model, this study analytically derives SFR characteristics and frequency stability indicators such as RoCoF, frequency nadir, and quasi-steady-state frequency deviation. A thorough investigation is conducted to quantify the impacts of load parameters including IM penetration rate, IM rotor inertia, and load level.

The rest of this paper is organized as follows. Section II presents detailed models of static and dynamic loads. Section III develops small-signal linearization models for power sources, power grid, and loads. In Section IV, the aggregated SFR model considering load dynamics is proposed and the impact of load parameters on frequency is analyzed. In Section V, case studies are presented to verify the accuracy of the proposed model. Finally, conclusions are drawn in Section VI.

II. Detailed Models of Static and Dynamic Loads

Future power systems are expected to evolve into a diversified structure encompassing generation, transmission, and loads, as illustrated in Fig. 1.

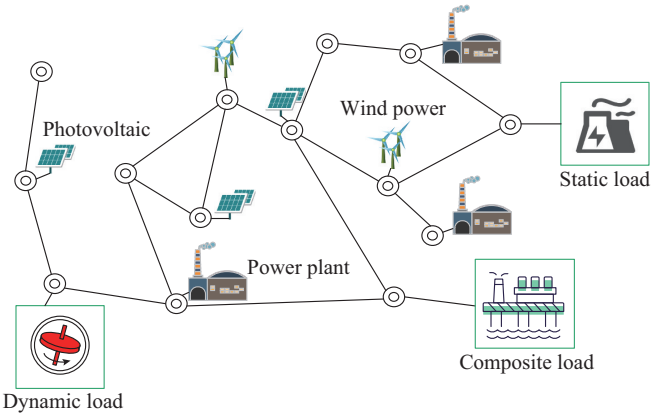

Fig. 1. Structure of future power systems with different types of loads.

In bulk power systems, loads can be broadly categorized into static, dynamic, and composite types. Static loads serve as generalized models that include classical CI, constant cur-

rent, and CP loads. In contrast, dynamic loads are primarily represented by IMs. To better capture the nodal characteristics of power loads, a CLM integrates both static and dynamic components. This model has been widely adopted in the grids of China and the United States [24], [25].

A. Static Load

The static load model is classically represented as:

$$\begin{cases} P_{\mathrm{s}} = P_{\mathrm{s0}}\left(V_{\mathrm{s}}/V_{\mathrm{s0}}\right)^{\alpha} \\ Q_{\mathrm{s}} = Q_{\mathrm{s0}}\left(V_{\mathrm{s}}/V_{\mathrm{s0}}\right)^{\beta} \end{cases} \tag{1}$$

where V_{s} is the voltage of the static load; P_{s} and Q_{s} are the active and reactive power of the static part of the load with voltage dependency exponents α and β, respectively; and P_{s0} and Q_{s0} are the initial active and reactive power of the static load, corresponding to the initial voltage V_{s0} of the static load, respectively. The type of static load is represented with parameters α and β (for CP load, $\alpha=\beta=0$; for constant current load, $\alpha=\beta=1$; for CI load $\alpha=\beta=2$).

B. Dynamic Load

The dynamic load is characterized by the classical third-order dynamic model, expressed as [26]:

$$\begin{cases} \dfrac{\mathrm{d}\omega_{\mathrm{r}}}{\mathrm{d}t} = -\dfrac{1}{2H_{\mathrm{IM}}}\left(T_{\mathrm{m}} - T_{\mathrm{e}}\right) \\ \dfrac{\mathrm{d}E'_q}{\mathrm{d}t} = -\dfrac{1}{\tau'_{d0}}\left[E'_q - \left(X - X_1\right)I_d\right] + \left(\omega_{\mathrm{r}} - 1\right)E'_d \\ \dfrac{\mathrm{d}E'_d}{\mathrm{d}t} = -\dfrac{1}{\tau'_{d0}}\left[E'_d + \left(X - X_1\right)I_q\right] - \left(\omega_{\mathrm{r}} - 1\right)E'_q \end{cases} \tag{2}$$

$$\begin{cases} I_d = \dfrac{1}{R_{\mathrm{s}}^2 + X_1^2}\left[R_{\mathrm{s}}\left(V_d - E'_d\right) + X_1\left(V_q - E'_q\right)\right] \\ I_q = \dfrac{1}{R_{\mathrm{s}}^2 + X_1^2}\left[R_{\mathrm{s}}\left(V_q - E'_q\right) - X_1\left(V_d - E'_d\right)\right] \end{cases} \tag{3}$$

$$\begin{cases} T_{\mathrm{m}} = \left(A_2\omega_{\mathrm{r}}^2 + A_1\omega_{\mathrm{r}} + A_0\right)T_{\mathrm{m0}} \\ T_{\mathrm{e}} = E'_d I_d + E'_q I_q \\ A_2 + A_1 + A_0 = 1 \end{cases} \tag{4}$$

where ω_{r} is the rotor speed of the machine in per unit; H_{IM}, T_{m}, T_{e}, and T_{m0} are the rotor inertia, mechanical torque, electromagnetic torque, and initial mechanical torque of the machine, respectively; $X = x_{\mathrm{s}} + x_{\mathrm{m}}$, $X_1 = x_{\mathrm{s}} + \left(x_{\mathrm{m}}x_{\mathrm{r}}\right)/\left(x_{\mathrm{m}} + x_{\mathrm{r}}\right)$, and x_{r}, x_{s}, and x_{m} are the rotor, stator, and magnetizing reactance of the machine, respectively; R_{r} is the rotor resistance; R_{s} is the stator resistance; $\tau'_{d0} = \left(x_{\mathrm{r}} + x_{\mathrm{m}}\right)/R_{\mathrm{r}}$ is the time constant; A_2 and A_1 are the speed-squared torque coefficient and linear drag coefficient, respectively; A_0 is the constant torque offset; E'_d and E'_q are the d-axis and q-axis transient electromotive forces of the machine, respectively; V_d and V_q are the d-axis and q-axis bus voltages, respectively; and I_d and I_q are the d-axis and q-axis stator currents, respectively.

Notably, the frequency stability discussed in this paper falls within the dynamic analysis of the electromechanical time scale. Consequently, the transient potential can be considered constant. Additionally, by neglecting power loss in the magnetizing branch, the relationship between the electromagnetic torque T_{e} and the slip rate s_{slip} of the asynchronous motor is approximated as:

$$T_{\mathrm{e}} = \frac{V_{\mathrm{IM}}^2 R_{\mathrm{r}}}{s_{\mathrm{slip}}\omega_{\mathrm{e}}\left[\left(R_{\mathrm{s}} + cR_{\mathrm{r}}/s_{\mathrm{slip}}\right)^2 + \left(x_{\mathrm{s}} + cx_{\mathrm{r}}\right)^2\right]} \tag{5}$$

where ω_{e} is the system frequency in per unit; $c = 1 + x_{\mathrm{r}}/x_{\mathrm{m}}$; $s_{\mathrm{slip}} = \left(\omega_{\mathrm{e}} - \omega_{\mathrm{r}}\right)/\omega_{\mathrm{e}}$; and V_{IM} is the stator voltage of the IM.

It can be observed from (5) that the electromagnetic torque of the IM is influenced not only by the rotor speed and grid angular speed, but also by the bus voltage. This indicates that the IM behaves as a voltage-sensitive load.

C. Composite Load

In practical power systems, loads include both static and dynamic components. To account for this, a CLM is adopted and is expressed as:

$$\begin{cases} P_{\mathrm{CLM}} = P_{\mathrm{s}} + P_{\mathrm{IM}} \\ Q_{\mathrm{CLM}} = Q_{\mathrm{s}} + Q_{\mathrm{IM}} \end{cases} \tag{6}$$

where P_{CLM} and Q_{CLM} are the active and reactive power of the composite load, respectively; and P_{IM} and Q_{IM} are the active and reactive power of the IM load, respectively.

Furthermore, the proportion of static load at the initial operating point of the system can be expressed as:

$$K_{\mathrm{sta}} = P_{\mathrm{s0}}/P_{\mathrm{CLM0}} \tag{7}$$

where P_{CLM0} is the load active power at the initial operating point.

III. Small-signal Linearization Models for Power Sources, Power Grid, and Loads

In power system modeling, frequency-active power dynamics are captured by ignoring the strong nonlinearities of all components and focusing on retaining the large time constants. This approach, as outlined in [27], has been recently applied to various elements, including those incorporating high-voltage direct current (HVDC) [28], wind turbines [29], and virtual synchronous generators [30]. All elements of the power system may contain weak nonlinear components, which can be appropriately linearized to simplify the solution and analysis of frequency dynamics.

A. Power Sources

The power system bus set is assumed to be $\Omega = \{i \in \mathbb{N} | i \leq n\} = \Omega_{\mathrm{G}} \cup \Omega_{\mathrm{L}}$, where Ω_{G} is the set of generation buses; Ω_{L} is the set of load buses, inside which Ω_{IM} is the set of IM buses; n is the number of system buses; and $\mathbb{N}$ is the set of natural numbers.

To model the synchronous generator i ($i \in \Omega_{\mathrm{G}}$), a second-order frequency response model is employed, which is shown in Fig. 2, where $\tau_{\mathrm{R}i}$ is the time constant of the reheating stage; $F_{\mathrm{H}i}$ is the power proportion coefficient of the high-pressure cylinder of the turbine; $R_{\mathrm{G}i}$ is the droop coefficient; $\Delta P_{\mathrm{Ge}i}$ is the electromagnetic power deviation; $\Delta P_{\mathrm{Gm}i}$ is the mechanical power deviation; $H_{\mathrm{G}i}$ is the rotor inertia; $\Delta\omega_{\mathrm{e}}$ is the deviation of ω_{e}; and $D_{\mathrm{G}i}$ is the damping coefficient.

The maximum power point tracking (MPPT) control for

grid-following RESs has the minimal response to system frequency, allowing their impact on power frequency to be neglected. In contrast, grid-forming RESs, which exhibit inertia to the system through virtual synchronous machine control, droop control, and matching control, can be analogized to synchronous generators [3]. Their linearization models can be aggregated into the multi-machine system. The aggregation method is detailed in [31] and will not be elaborated here due to space limitations.

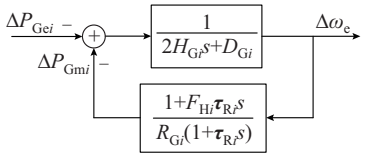

Fig. 2. Second-order frequency response model of synchronous generator.

B. Power Grid

Active power disturbances can alter the current distribution in the power grid and consequently influence bus voltages. This phenomenon becomes particularly pronounced in systems with weak voltage strength that contain substantial voltage-sensitive loads, where even minor voltage variations can induce considerable changes in the active power of the loads. The behavior of the power grid can be mathematically represented using static power flow equations. Equation (8) describes the linearization relationship between load bus voltage and active power variation.

$$\Delta \boldsymbol{v}_{\mathrm{L}} = \boldsymbol{k}_{\mathrm{sens},k}\Delta P_k \tag{8}$$

where ΔP_k is the active power variation at bus k ($k \in \Omega$); $\Delta \boldsymbol{v}_{\mathrm{L}}$ is the column vector of load bus voltage variations; and $\boldsymbol{k}_{\mathrm{sens},k}$ is the sensitivity column vector of load voltage magnitude to active power variation at bus k.

For a change in active power at bus k, the term $k_{\mathrm{sens},ik}$ for load bus i ($i \in \Omega_{\mathrm{L}}$) can be obtained by inverting the Jacobian matrix, expressed as:

$$k_{\mathrm{sens},ik} = \frac{\partial V_{\mathrm{L}i}}{\partial P_k} \tag{9}$$

where $V_{\mathrm{L}i}$ is the voltage magnitude at load bus i; and P_k is the active power at bus k.

C. Loads

Based on the CLM discussed in Section II, the power variation of the static part is expressed as:

$$\begin{cases} \Delta P_{\mathrm{s}} = g_{\mathrm{SVP}}\Delta V_{\mathrm{s}} \\ g_{\mathrm{SVP}} = \dfrac{\alpha P_{\mathrm{s0}}}{V_{\mathrm{s0}}} \end{cases} \tag{10}$$

where ΔP_{s} is the deviation of P_{s}; g_{SVP} is the active power-voltage gain of the static part; and ΔV_{s} is the deviation of V_{s}.

The small-signal linearization equations of the IM can be represented with reference to (2)-(5) as:

$$\frac{\mathrm{d}\Delta\omega_{\mathrm{r}}}{\mathrm{d}t} = -\frac{1}{2H_{\mathrm{IM}}}\left(\Delta T_{\mathrm{m}} - \Delta T_{\mathrm{e}}\right) \tag{11a}$$

$$\Delta T_{\mathrm{m}} = K_{T_{\mathrm{m}},\omega_{\mathrm{r}}} T_{\mathrm{m0}}\Delta\omega_{\mathrm{r}} \tag{11b}$$

$$\Delta T_{\mathrm{e}} = K_{T_{\mathrm{e}},\omega_{\mathrm{e}}}\Delta\omega_{\mathrm{e}} + K_{T_{\mathrm{e}},\omega_{\mathrm{r}}}\Delta\omega_{\mathrm{r}} + K_{T_{\mathrm{e}},V_{\mathrm{IM}}}\Delta V_{\mathrm{IM}} \tag{11c}$$

$$\Delta P_{\mathrm{IM}} = T_{\mathrm{e0}}\Delta\omega_{\mathrm{e}} + \omega_{\mathrm{e0}}\Delta T_{\mathrm{e}} \tag{11d}$$

where $\Delta\omega_{\mathrm{r}}$, ΔT_{m}, ΔT_{e}, and ΔV_{IM} are the deviations of ω_{r}, T_{m}, T_{e}, and V_{IM}, respectively; ΔP_{IM} is the deviation of P_{IM}; ω_{r0} is the initial value of the rotor speed of the IM; T_{e0} is the initial electromagnetic torque of the IM; ω_{e0} is the initial system frequency; and the coefficients $K_{T_{\mathrm{m}},\omega_{\mathrm{r}}}$, $K_{T_{\mathrm{e}},\omega_{\mathrm{e}}}$, $K_{T_{\mathrm{e}},\omega_{\mathrm{r}}}$, and $K_{T_{\mathrm{e}},V_{\mathrm{IM}}}$ are defined as:

$$\begin{cases} K_{T_{\mathrm{m}},\omega_{\mathrm{r}}} = \left.\dfrac{\partial T_{\mathrm{m}}}{\partial\omega_{\mathrm{r}}}\right|_{\omega_{\mathrm{r}}=\omega_{\mathrm{r0}}} = 2A_2\omega_{\mathrm{r0}} + A_1 \\ K_{T_{\mathrm{e}},\omega_{\mathrm{e}}} = \left.\dfrac{\partial T_{\mathrm{e}}}{\partial\omega_{\mathrm{e}}}\right|_{\omega_{\mathrm{e}}=\omega_{\mathrm{e0}}} = \dfrac{T_{\mathrm{e0}}}{\omega_{\mathrm{e0}}-\omega_{\mathrm{r0}}}\left[1-2\dfrac{R_{\mathrm{sr}}\left(R_{\mathrm{s}}+R_{\mathrm{r}}/s_{\mathrm{slip0}}\right)+x_{\mathrm{sr}}^2}{\left(R_{\mathrm{s}}+R_{\mathrm{r}}/s_{\mathrm{slip0}}\right)^2+x_{\mathrm{sr}}^2}\right] \\ K_{T_{\mathrm{e}},\omega_{\mathrm{r}}} = \left.\dfrac{\partial T_{\mathrm{e}}}{\partial\omega_{\mathrm{r}}}\right|_{\omega_{\mathrm{r}}=\omega_{\mathrm{r0}}} = -\dfrac{T_{\mathrm{e0}}}{\omega_{\mathrm{e0}}-\omega_{\mathrm{r0}}}\left[1-2\dfrac{R_{\mathrm{s}}\left(R_{\mathrm{s}}+R_{\mathrm{r}}/s_{\mathrm{slip0}}\right)+x_{\mathrm{sr}}^2}{\left(R_{\mathrm{s}}+R_{\mathrm{r}}/s_{\mathrm{slip0}}\right)^2+x_{\mathrm{sr}}^2}\right] \\ K_{T_{\mathrm{e}},V_{\mathrm{IM}}} = \left.\dfrac{\partial T_{\mathrm{e}}}{\partial V_{\mathrm{IM}}}\right|_{V_{\mathrm{IM}}=V_{\mathrm{IM0}}} = \dfrac{2T_{\mathrm{e0}}}{V_{\mathrm{IM0}}} \end{cases} \tag{12}$$

where s_{slip0} and V_{IM0} are the initial slip ratio and initial stator voltage of the IM, respectively; $R_{\mathrm{sr}} = R_{\mathrm{r}} + R_{\mathrm{s}}$; and $x_{\mathrm{sr}} = x_{\mathrm{s}} + x_{\mathrm{r}}$.

From (12), it is evident that $K_{T_{\mathrm{m}},\omega_{\mathrm{r}}} > 0$ and $K_{T_{\mathrm{e}},V_{\mathrm{IM}}} > 0$, indicating that the IM also contains a CI load component. For IM with high power, the slip rate $s_{\mathrm{slip0}} < 1\%$ [32], and it is observed that $K_{T_{\mathrm{e}},\omega_{\mathrm{e}}} > 0$ and $K_{T_{\mathrm{e}},\omega_{\mathrm{r}}} < 0$. The related proof can be found in Appendix A.

By substituting (11b) and (11c) into (11a), and then organizing and transforming it into the complex frequency domain, the following expression is obtained:

$$\Delta\omega_{\mathrm{r}}(s) = \frac{K_{T_{\mathrm{e}},\omega_{\mathrm{e}}}\Delta\omega_{\mathrm{e}}(s) + K_{T_{\mathrm{e}},V_{\mathrm{IM}}}\Delta V_{\mathrm{IM}}(s)}{2H_{\mathrm{IM}}s + K_{T_{\mathrm{m}},\omega_{\mathrm{r}}} - K_{T_{\mathrm{e}},\omega_{\mathrm{r}}}} \tag{13}$$

By elaborating (13) with (11c) and (11d), the following expression is obtained:

$$\Delta P_{\mathrm{IMe}}(s) = g_{\mathrm{DFP}}(s)\Delta\omega_{\mathrm{e}}(s) + g_{\mathrm{DVP}}(s)\Delta V_{\mathrm{IM}}(s) \tag{14a}$$

$$\begin{cases} g_{\mathrm{DFP}}(s) = T_{\mathrm{e0}} + K_{T_{\mathrm{e}},\omega_{\mathrm{e}}} + \dfrac{K_{T_{\mathrm{e}},\omega_{\mathrm{r}}}K_{T_{\mathrm{e}},\omega_{\mathrm{e}}}}{2H_{\mathrm{IM}}s + K_{T_{\mathrm{m}},\omega_{\mathrm{r}}} - K_{T_{\mathrm{e}},\omega_{\mathrm{r}}}} \\ g_{\mathrm{DVP}}(s) = K_{T_{\mathrm{e}},V_{\mathrm{IM}}} + \dfrac{K_{T_{\mathrm{e}},\omega_{\mathrm{r}}}K_{T_{\mathrm{e}},V_{\mathrm{IM}}}}{2H_{\mathrm{IM}}s + K_{T_{\mathrm{m}},\omega_{\mathrm{r}}} - K_{T_{\mathrm{e}},\omega_{\mathrm{r}}}} \end{cases} \tag{14b}$$

From (14a), it is observed that the dynamic impact of the IM on the active power of the system can be described by considering the following three aspects.

1) Voltage-active power dynamics. The disturbance affects the voltage magnitude at the IM bus. This causes a direct change in the active power of the IM. It is considered as a CI load effect due to the bus voltage variation.

2) Frequency-active power dynamics. Variations in the system frequency induce the IM to simultaneously produce instantaneous and steady-state active power (damping term), thereby compensating for the inherent power imbalance within the system.

3) Inertia contribution. Inertia measures the ability to

maintain the state variables of an element unchanged. The imbalance power at the IM bus causes some changes in the IM rotor kinetic energy, resisting changes in electromagnetic power. The inertia contribution provided by the IM is analyzed and discussed in Section IV.

Based on (10) and (14a), the active power variations of composite load can be categorized into three components: load voltage dynamics, load frequency dynamics, and load inertia contribution.

IV. Aggregated SFR Model Considering Load Dynamics and Impact of Load Parameters on Frequency

Based on the linearization models of loads established in Section III, a general and aggregated SFR model considering different types of load dynamics is developed in this section.

A. General SFR Model Considering Load Dynamics

The general SFR model considering load dynamics for the multi-machine system is shown in Fig. 3, where ΔP_{VL} and ΔP_{fL} are the active power variations of voltage dynamics and frequency dynamics, respectively; ΔP_{Gm} is the mechanical power deviation; H_{L} is the load inertia; $\boldsymbol{g}_{\mathrm{LVP}}(s)$ and $\boldsymbol{g}_{\mathrm{DFP}}(s)$ are the column vectors of active power-voltage gain and active power-frequency gain, respectively; H_{G} is the rotor inertia of synchronous generator; D_{G} is the damping coefficient of synchronous generator; τ_{R} is the time constant of the reheating stage; F_{H} is the power proportion coefficient for the high-pressure cylinder of the turbine; and R_{G} is the droop coefficient of synchronous generator.

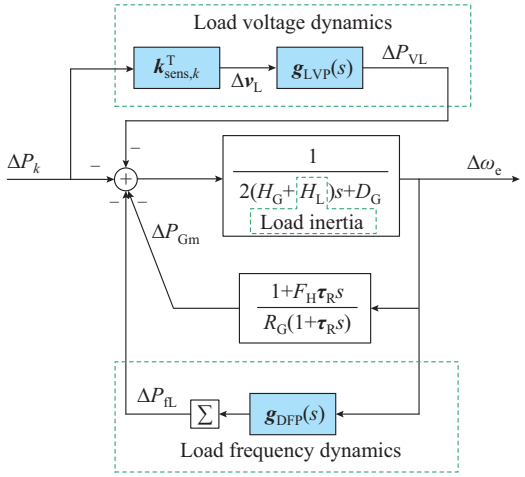

Fig. 3. General SFR model considering load dynamics for multi-machine system.

As summarized in Section III, the impact of loads on the SFR can be classified into three different components, i.e., load voltage dynamics, load frequency dynamics, and load inertia contribution.

1) Load Voltage Dynamics

The load voltage dynamics result from the combined effect of CI loads and IM. The variation in active power is expressed as:

$$\begin{cases} \Delta P_{V,\mathrm{load}}(s) = \Delta P_k\left(\boldsymbol{k}^{\mathrm{T}}_{\mathrm{sens},k}\boldsymbol{g}_{\mathrm{LVP}}(s)\right) \\ g_{\mathrm{LVP}i}(s) = K_{\mathrm{S}}\left(g_{\mathrm{SVP}i} + K_{\mathrm{IM}i}g_{\mathrm{DVP}i}(s)\right) \\ K_{\mathrm{IM}i} = S_{\mathrm{IM}i}/S_{\mathrm{B}} \\ K_{\mathrm{S}} = S_{\mathrm{B}}/\sum_{j\in\Omega_{\mathrm{G}}} S_{\mathrm{G}j} \end{cases} \tag{15}$$

where $g_{\mathrm{LVP}i}(s)$ is the active power-voltage gain of the i^{th} ($i\in\Omega_{\mathrm{L}}$) load; $g_{\mathrm{SVP}i}$ and $g_{\mathrm{DVP}i}(s)$ are the active power-voltage gains of the static part and dynamic part of the i^{th} load, respectively; $K_{\mathrm{IM}i}$ is the ratio of the capacity of the i^{th} IM to base capacity; K_{S} is the ratio of base capacity to total system capacity; S_{B} is the base capacity; and $S_{\mathrm{IM}i}$ and $S_{\mathrm{G}j}$ are the capacities of the i^{th} IM and the j^{th} synchronous generator, respectively.

From the above equation, it appears that the impact of load voltage dynamics on the active power of the system mainly depends on three aspects: ① the magnitude of the active power variation ΔP_k; ② the voltage sensitivity to active power variations $k_{\mathrm{sens},ik}$, which is related to the electrical distance between the active power variation buses and the voltage-sensitive load; and ③ the load active power sensitivity to bus voltage variation $g_{\mathrm{LVP}i}$. The higher ΔP_k and $g_{\mathrm{LVP}i}$, with a shorter electrical distance (i.e., higher $k_{\mathrm{sens},ik}$) between the active power variation buses and the voltage-sensitive load, result in a more significant influence of load voltage dynamics.

2) Load Frequency Dynamics

Load frequency dynamics are caused by the IM, and the variation in active power is expressed as:

$$\Delta P_{f,\mathrm{load}}(s) = \Delta\omega_{\mathrm{e}}\sum_{i\in\Omega_{\mathrm{IM}}} g_{\mathrm{DFP}i}(s) \tag{16}$$

where $g_{\mathrm{DFP}i}(s)$ is the active power-frequency gain of the i^{th} ($i\in\Omega_{\mathrm{L}}$) load, which is expressed as:

$$g_{\mathrm{DFP}i}(s) = K_{\mathrm{IM}i}\frac{1+F_{\mathrm{IM}i}\tau_{\mathrm{IM}i}s}{R_{\mathrm{IM}i}\left(1+\tau_{\mathrm{IM}i}s\right)} \tag{17}$$

where $\tau_{\mathrm{IM}i}$ is the time constant of the i^{th} ($i\in\Omega_{\mathrm{IM}}$) IM; $F_{\mathrm{IM}i}$ is the power proportion coefficient of the i^{th} IM; and $R_{\mathrm{IM}i}$ is the droop coefficient of the i^{th} IM.

$$\begin{cases} \tau_{\mathrm{IM}i} = \dfrac{2H_{\mathrm{IM}i}}{K_{T_{\mathrm{m}},\omega_{\mathrm{r}},i} - K_{T_{\mathrm{e}},\omega_{\mathrm{r}},i}} \\ R_{\mathrm{IM}i} = \dfrac{K_{T_{\mathrm{m}},\omega_{\mathrm{r}},i} - K_{T_{\mathrm{e}},\omega_{\mathrm{r}},i}}{\left(T_{\mathrm{e}0i}+K_{T_{\mathrm{e}},\omega_{\mathrm{e}},i}\right)\left(K_{T_{\mathrm{m}},\omega_{\mathrm{r}},i} - K_{T_{\mathrm{e}},\omega_{\mathrm{r}},i}\right) + K_{T_{\mathrm{e}},\omega_{\mathrm{r}},i}K_{T_{\mathrm{e}},\omega_{\mathrm{e}},i}} \\ F_{\mathrm{IM}i} = \left(T_{\mathrm{e}0i}+K_{T_{\mathrm{e}},\omega_{\mathrm{e}},i}\right)R_{\mathrm{IM}i} \end{cases} \tag{18}$$

where $H_{\mathrm{IM}i}$ and $T_{\mathrm{e}0i}$ are the rotor inertia and initial electromagnetic torque of the i^{th} ($i\in\Omega_{\mathrm{IM}}$) IM, respectively; $K_{T_{\mathrm{m}},\omega_{\mathrm{r}},i}$, $K_{T_{\mathrm{e}},\omega_{\mathrm{r}},i}$, and $K_{T_{\mathrm{e}},\omega_{\mathrm{e}},i}$ are the sensitivity coefficients of the i^{th} ($i\in\Omega_{\mathrm{IM}}$) CLM.

3) Load Inertia Contribution

According to [6], the load inertia is expressed as:

$$H_{\mathrm{L}i} = \frac{J_i\omega_{ri}^2/2}{S_{\mathrm{B}}} \tag{19}$$

where $H_{\mathrm{L}i}$, J_i, and ω_{ri} are the inertia, moment of inertia, and

rotor speed of the i^{th} ($i \in \Omega_{\text{L}}$) load, respectively.

B. Aggregated SFR Model Considering Load Dynamics

The aggregation of multi-machine systems is performed using the method described in [9], where all power sources and loads are represented by a capacity-weighted approach. The approximate analytical model of the aggregated SFR model considering load dynamics is shown in Fig. 4, where $G_{\text{V},k}$ is the voltage dynamic gain under active power variation at bus k; ΔP_{e} and ΔP_{m} are the electromagnetic power deviation and mechanical power deviation of the aggregated SFR model, respectively; and H_{e}, D_{e}, R_{e}, τ_{e}, and F_{e} are the inertia, damping coefficient, droop coefficient, time constant, and power proportion coefficient of the power system, respectively.

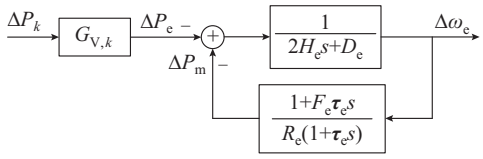

Fig. 4. Approximate analytical model of aggregated SFR model considering load dynamics.

The system damping is primarily provided by the generators, while the system inertia is contributed by both synchronous generators and IM. The system inertia H_{e} is defined as:

$$H_{\text{e}} = \frac{\sum_{i \in \Omega_{\text{G}}} H_{\text{G}i} S_{\text{G}i}}{\sum_{i \in \Omega_{\text{G}}} S_{\text{G}i}} + \sum_{i \in \Omega_{\text{L}}} H_{\text{L}i} \tag{20}$$

The disturbance in the system is considered as step change at the variation point. The voltage time constant depends on excitation control, loads, and power grid parameters. In general, it is possible to approximate load voltage changes as step dynamics. This is because the transient voltage time constant (millisecond scale) is much smaller than the electromechanical time scale. Therefore, $G_{\text{V},k}$ and $g_{\text{LVP}i}$ are approximated as:

$$\begin{cases} G_{\text{V},k} = 1 + \boldsymbol{k}_{\text{sens},k}^{\text{T}} \boldsymbol{g}_{\text{LVP}} \\ g_{\text{LVP}i} = K_{\text{S}} \left(g_{\text{SVP},i} + K_{\text{IM}i} K_{T_{\text{e}}, V_{\text{IM}}, i} \right) \end{cases} \tag{21}$$

where $K_{T_{\text{e}}, V_{\text{IM}}, i}$ is the first-order partial derivative of the electromagnetic torque of the i^{th} ($i \in \Omega_{\text{IM}}$) IM with respect to the stator voltage.

The constant gain K_m and normalized gain λ_m are defined as:

$$\begin{cases} K_m = \dfrac{S_m}{\sum_{i \in \Omega_{\text{G}}} S_{\text{G}i}} \quad m \in \Omega \\ \lambda_m = \dfrac{\kappa_m}{\sum_{m \in \Omega} \kappa_m} \end{cases} \tag{22}$$

where S_m is the capacity of the m^{th} ($m \in \Omega$) device; and $\kappa_m = K_m / R_m$, and R_m is the droop coefficient of the m^{th} ($m \in \Omega$) device.

On these bases, the equivalent prime mover-governor section is aggregated as:

$$\begin{cases} \dfrac{1}{R_{\text{e}}} = \sum_{m \in \Omega} \kappa_m = \sum_{i \in \Omega_{\text{G}}} \dfrac{K_i}{R_{\text{G}i}} + \sum_{j \in \Omega_{\text{IM}}} \dfrac{K_j}{R_{\text{IM}j}} \\ F_{\text{e}} = \sum_{m \in \Omega} \lambda_m F_m = R_{\text{e}} \left(\sum_{i \in \Omega_{\text{G}}} \dfrac{K_i F_{\text{H}i}}{R_{\text{G}i}} + \sum_{j \in \Omega_{\text{IM}}} \dfrac{K_j F_{\text{IM}j}}{R_{\text{IM}j}} \right) \\ \tau_{\text{e}} = \sum_{m \in \Omega} \lambda_m T_m = R_{\text{e}} \left(\sum_{i \in \Omega_{\text{G}}} \dfrac{K_i \tau_{\text{R}i}}{R_{\text{G}i}} + \sum_{j \in \Omega_{\text{IM}}} \dfrac{K_j \tau_{\text{IM}j}}{R_{\text{IM}j}} \right) \end{cases} \tag{23}$$

where K_i is the i^{th} ($i \in \Omega$) constant gain; F_m and T_m are the power proportion coefficient and time constant of the m^{th} ($m \in \Omega$) device, respectively; and $F_{\text{IM}j}$, $R_{\text{IM}j}$, and $\tau_{\text{IM}j}$ are the power proportion coefficient, droop coefficient, and time constant of the j^{th} ($j \in \Omega_{\text{IM}}$) IM, respectively.

Based on the established aggregated SFR model, the three frequency stability indicators are determined as:

$$RoCoF_{\max} = \left(\frac{\text{d}\omega_{\text{s}}}{\text{d}t} \right)_{\max} = \left| \frac{G_{\text{V},k} \Delta P_k \omega_{\text{en}}}{2H_{\text{e}}} \right| \tag{24a}$$

$$\begin{cases} \Delta\omega_{\max} = \left| \dfrac{G_{\text{V},k} \Delta P_k}{D_{\text{e}} + 1/R_{\text{e}}} \left(1 + \text{e}^{-\xi \omega_{\text{n}} t_{\text{nadir}}} \sqrt{\dfrac{\tau_{\text{e}}(1 - F_{\text{e}})}{2H_{\text{e}} + R_{\text{e}}}} \right) \right| \\ t_{\text{nadir}} = \dfrac{1}{\omega_{\text{n}} \sqrt{1 - \xi^2}\, D_{\text{e}} + 1/R_{\text{e}}} \arctan \left(\dfrac{\omega_{\text{n}} \sqrt{1 - \xi^2}\, \tau_{\text{e}}}{\xi \omega_{\text{n}} \tau_{\text{e}} - 1} \right) \end{cases} \tag{24b}$$

$$\Delta\omega_{\text{qss}} = \left| \frac{G_{\text{V},k} \Delta P_k}{D_{\text{e}} + 1/R_{\text{e}}} \right| \tag{24c}$$

$$\begin{cases} \omega_{\text{n}} = \sqrt{\left(R_{\text{e}} D_{\text{e}} + 1 \right) / \left(2H_{\text{e}} \tau_{\text{e}} R_{\text{e}} \right)} \\ \xi = \left(2H_{\text{e}} R_{\text{e}} + D_{\text{e}} \tau_{\text{e}} R_{\text{e}} + F_{\text{e}} \tau_{\text{e}} \right) / \left(4H_{\text{e}} \tau_{\text{e}} R_{\text{e}} \omega_{\text{n}} \right) \end{cases} \tag{25}$$

where $RoCoF_{\max}$ is the maximum RoCoF; $\Delta\omega_{\max}$ and t_{nadir} are the maximum frequency deviation and the time at which it occurs, respectively; $\Delta\omega_{\text{qss}}$ is the quasi-steady-state frequency deviation; ω_{en} is the base frequency; and ω_{n} and ξ are the undamped natural frequency and damping ratio, respectively.

Thus, a low-order aggregated SFR model of the system, accounting for the dynamic impact of the load, is obtained.

From (18) to (24), it can be observed that $RoCoF_{\max}$ is related to the load inertia and the voltage dynamic gain $G_{\text{V},k}$. The greater the load inertia and the voltage dynamic gain, the lower the $RoCoF_{\max}$. The maximum frequency deviation has a nonlinear relationship with the load inertia, IM droop coefficient, and IM penetration rate. The quasi-steady-state frequency deviation is basically related to the IM droop coefficient. Additionally, $G_{\text{V},k}$ directly influences the imbalance power of the system, subsequently affecting the three frequency stability indicators.

V. Case Study

In this section, the WECC 9-bus test system is utilized as an example, which includes converter-interfaced generation (CIG) and doubly-fed induction generator (DFIG). A time-domain simulation model is built in MATLAB/Simulink. The structure of this test system is shown in Fig. 5. To verify accuracy of the results, the frequency response of the pro-

posed model is compared with those of the traditional SFR model and the time-domain simulation model.

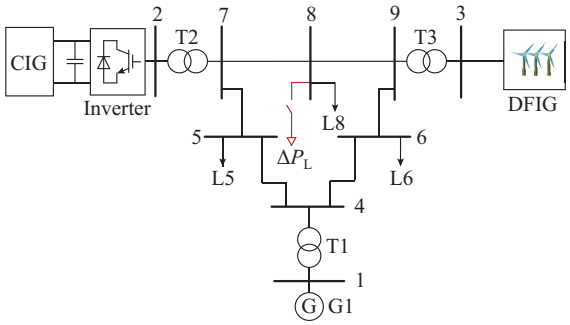

Fig. 5. Structure of WECC 9-bus test system.

The parameters of the generator G1 and power network in Fig. 5 are shown in [33], and the generator is in automatic voltage regulation mode. The capacities of CIG and DFIG are 192 MVA and 128 MVA, respectively, whose parameters are described in [1]. The total load is 200 MW. The penetration rate of power electronic sources is 56.4%. This indicates that the modified WECC 9-bus test system exhibits typical characteristics of future power systems.

It should be noted that CIG and DFIG contribute minimal inertial response and primary frequency regulation, as they predominantly operate in CP control mode. To analyze system behavior under varying conditions, five distinct cases are established, as shown in Fig. 6. The key parameters of the IM are provided in Table I.

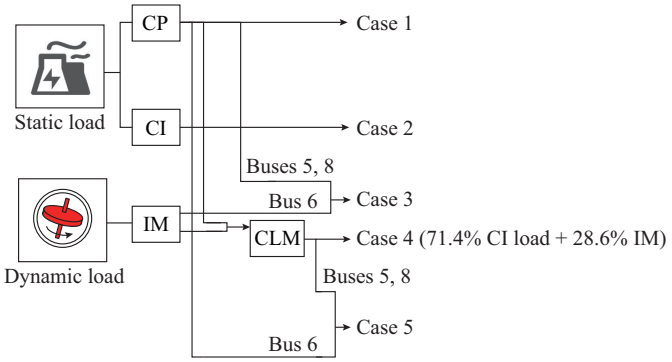

Fig. 6. Cases setting under different load types or combinations

TABLE I
KEY PARAMETERS OF IM

Parameter	Value
R_s, R_r	0.2 p.u., 0.02 p.u.
x_s, x_r, x_m	0.18 p.u., 0.12 p.u., 3.5 p.u.
H_{IM}	1 s
A_2, A_1, A_0	0.85, 0, 0.2038

A. Accuracy Validation of Proposed Model

The parameters calculated from the proposed model are shown in Table II.

At $t=150$ s, a 15 MW load disturbance is applied at bus 8. The frequency responses of the proposed model and time-domain simulation model (denoted as Model 1) are compared in five cases, as shown in Fig. 7(a). The results of traditional SFR model (denoted as Model 2) serve as the benchmark for frequency response accuracy. Furthermore, the superiority of the proposed model is demonstrated by comparing the maximum frequency errors e_{max} between its analytical solutions and those of Model 2, as shown in Fig. 7(b). Since the CP load in Case 1 does not depend on voltage, the proposed model in Case 1 is identical to Model 2 in all cases.

TABLE II
PARAMETERS CALCULATED FROM PROPOSED MODEL

Parameter	Value
$k_{sens,58}$, $k_{sens,68}$, $k_{sens,88}$	−0.014, −0.0158, −0.0435
K_{T_m,ω_r}, K_{T_e,ω_r}, K_{T_e,ω_s}, $K_{T_e,V_{IM}}$	0.7136, −31.4843, 30.713, 0.8359
τ_{IM}	0.0621 s
R_{IM}	0.8972
F_{IM}	27.94

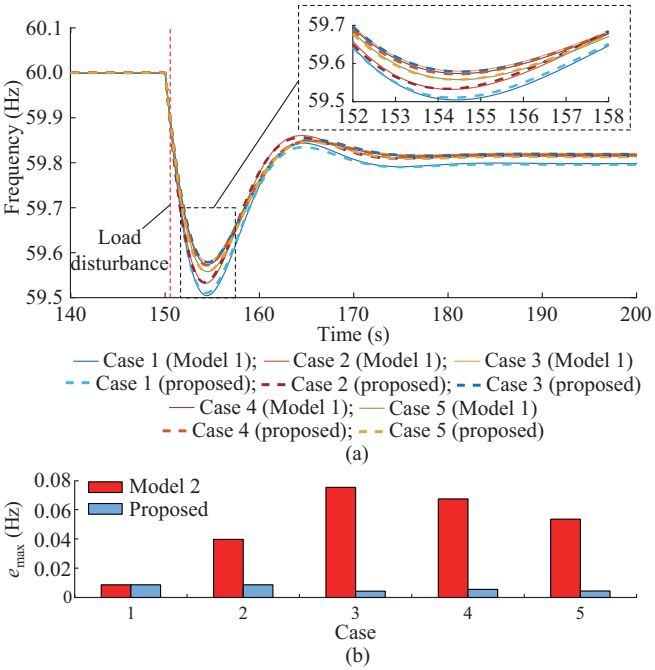

Fig. 7. Frequency response and the maximum frequency error comparison of different models in five cases. (a) Frequency response comparison. (b) The maximum frequency error comparison.

The comparison of frequency stability indicators for five cases is presented in Table III.

From Fig. 7, the five cases exhibit different frequency response characteristics. Different types or combinations of loads have significant impacts on the SFR. In all the cases, Model 2 shows e_{max} of 0.075 Hz, while the proposed model achieves superior accuracy with $e_{max} \leq 0.008$ Hz, demonstrating that the proposed model can reflect the active power variations of all the loads. For the three frequency stability indicators in Table III, the difference between Model 1 and the proposed model is very small, indicating that the proposed model has high accuracy.

TABLE III
COMPARISONS OF FREQUENCY STABILITY INDICATORS FOR FIVE CASES

Case	$RoCoF_{max}$ (Hz·s^{-1})		$\Delta\omega_{max}$ (Hz)		$\Delta\omega_{qss}$ (Hz)	
	Model 1	Proposed	Model 1	Proposed	Model 1	Proposed
1	0.210	0.212	0.495	0.489	0.202	0.204
2	0.185	0.186	0.468	0.466	0.183	0.185
3	0.145	0.153	0.420	0.421	0.179	0.181
4	0.138	0.145	0.425	0.428	0.181	0.182
5	0.152	0.158	0.442	0.442	0.186	0.187

At the same time, Fig. 7 and Table III indicate that Case 1 shows the worst performance, displaying the largest $RoCoF_{max}$ and frequency deviation. Case 2 shows lower $\Delta\omega_{max}$ and $RoCoF_{max}$ compared to those of Case 1, which is due to the voltage dynamics of CI load. Case 3 and Case 4 have the most significant inhibition of transient frequencies, which is a result of the role of voltage dynamics from CI load and IMs, and frequency dynamics and inertia contributions from IMs. The slight difference in frequency response between Case 3 and Case 4 can be approximately neglected. The frequency in Case 5 changes more rapidly than that in Case 4 due to the replacement of the composite load with a CP load at bus 6.

Overall, the CP load has no impact on the SFR. Both CI load and IM contain voltage dynamics, which directly and linearly produce active power increments. This indicates that voltage dynamics act as a rapid automatic load control, similar to automatic generation control. The primary frequency regulation effect of the IM ($\sum_{m\in\Omega_{IM}}\kappa_m=0.47$) is significantly smaller than that of the generator ($\sum_{m\in\Omega_G}\kappa_m=8.7$) and can thus be neglected. Furthermore, the inertia contribution of IM is evident when comparing Case 3 with Case 2.

To further analyze the impact of different types of loads on system frequency, the active power variations of load buses in five cases are compared, as shown in Fig. 8.

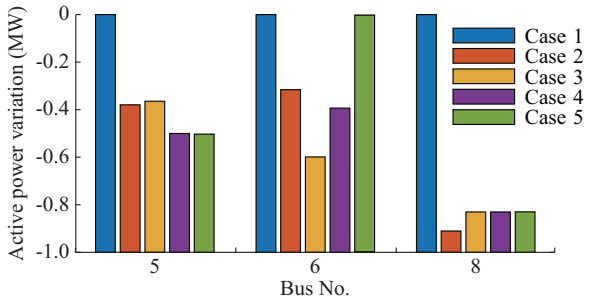

Fig. 8. Active power variations of load buses in five cases.

From Fig. 8, the CP loads in Case 1 exhibit negligible active power variations, while the CI loads with voltage dynamics in Case 2 show significant active power responses. Notably, since the perturbation point is set at bus 8, the voltage sensitivity to active power variations $k_{sens,88}$ is the largest among all load buses, resulting in the largest active power variation at bus 8. In Case 3, the active power variations at buses 5 and 8 remain similar to those in Case 2. However, the active power variation at bus 6, dominated by IM, becomes more pronounced, leading to a larger active power variation in total load in Case 3. In Case 4, the distributed integration of IMs across multiple load buses amplifies active power variations at each bus compared to Case 2. Comparing Case 5 with Case 4, there is no difference in the active power variations at buses 5 and 8, except that the CP at bus 6 has almost no power response. Overall, Case 3 and Case 4 have the largest active power variation (2.1 MW) in total load, which is a good indication of the extent to which IM has a greater impact on the system frequency compared with other loads.

B. Accuracy Verification of Proposed Model in Other Operational Scenarios

Three scenarios are set based on Case 4, in which all loads are composite loads (71.4% CI load + 28.6% IM). These scenarios further demonstrate the applicability and effectiveness of the proposed model.

1) Scenario 1: IM penetration rates of 10%, 30%, and 50% are selected. The calculation results of the relevant parameters under different IM penetration rates are shown in Table IV. With the increase in the IM penetration rate, the contributions of IM to inertia, primary frequency regulation, and voltage dynamics become more pronounced. When the IM penetration rate reaches 50%, the inertia contribution accounts for 13.8% of the total system inertia. Meanwhile, the IM delay time constant τ_{IM} decreases. Higher IM penetration rates result in greater frequency regulation contributions.

TABLE IV
CALCULATION RESULTS OF RELEVANT PARAMETERS UNDER DIFFERENT IM PENETRATION RATES

Parameter	Value		
	10%	30%	50%
K_{T_m,ω_r}	0.428	0.714	1.286
K_{T_e,ω_r}	–15.742	–31.484	–56.672
K_{T_e,ω_e}	15.357	30.713	55.284
$K_{T_e,V_{IM}}$	0.4179	0.8360	1.5050
τ_{IM} (s)	0.1240	0.0621	0.0350
R_{IM}	1.7900	0.8972	0.4980
F_{IM}	27.94	27.94	27.94
H_L (s)	0.187	0.455	0.680

The comparison of frequency responses of the proposed model and Model 1, as well as the maximum frequency error of the proposed model under different IM penetration rates are shown in Fig. 9.

Figure 8 illustrates that as the IM penetration rate gradually increases, the active power-voltage gain g_{LVP} and the primary frequency regulation gain of loads ($1/R_{IM}$) increase, while the time constant τ_{IM} decreases. In addition, the system inertia H_e increases with the IM penetration rate. This indicates that with the increase of IM penetration rate, all three influencing factors enhance the frequency support capability, and the proposed model accurately reflects these dynamic

characteristics. Additionally, $\Delta\omega_{qss}$ under different IM penetration rates exhibit minimal variation, indicating that $1/R_{IM}$ of the load is relatively small compared with that of the governor.

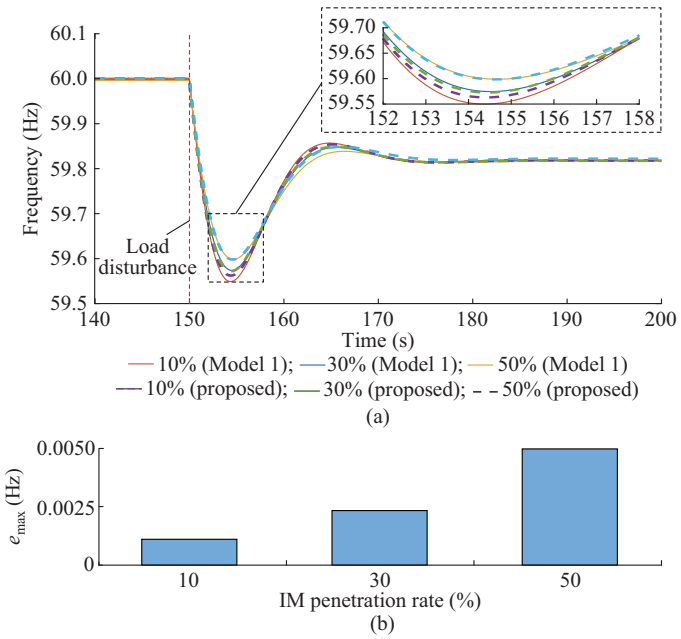

Fig. 9. Comparison of frequency responses of proposed model and Model 1 and the maximum frequency error of proposed model under different IM penetration rates. (a) Comparison of frequency responses. (b) The maximum frequency error of proposed model.

2) Scenario 2: IM rotor inertias of 1, 3, and 5 s are selected. According to (18) and (19), the IM rotor inertia affects the time constant τ_{IM} and the load inertia H_L. The calculation results of relevant parameters under different IM rotor inertia are shown in Table V.

TABLE V
CALCULATION RESULTS OF RELEVANT PARAMETERS UNDER DIFFERENT IM ROTOR INERTIA

Parameter	Value		
	1 s	3 s	5 s
τ_{IM} (s)	0.0621	0.1860	0.3110
H_L (s)	0.4550	1.3690	2.2810

Table V shows that the higher IM rotor inertia increases the stored rotor kinetic energy under rated operating conditions. This means that the IM rotor inertia positively contributes to the system synchronous inertia. However, it also results in an increase in the time constant τ_e of power system.

A comparison of frequency responses of the proposed model and Model 1 and the maximum frequency error of the proposed model under different IM rotor inertia are shown in Fig. 10. $\Delta\omega_{max}$ and $RoCoF_{max}$ are changing according to Fig. 10. It can be inferred from (19) and (20) that the system synchronous inertia is significantly enhanced by increasing the IM rotor inertia. Thus, the proposed model effectively reflects these dynamic characteristics.

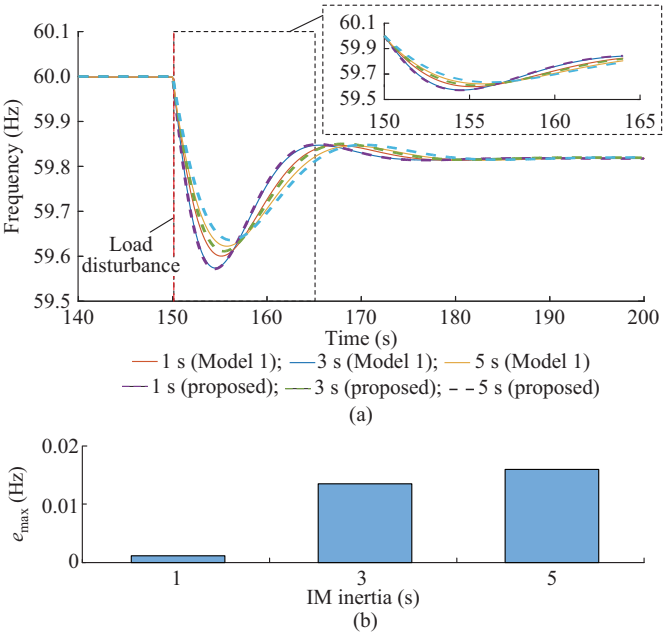

Fig. 10. Comparison of frequency responses of proposed model and Model 1 and the maximum frequency error of proposed model under different IM rotor inertia. (a) Comparison of frequency responses. (b) The maximum frequency error of proposed model.

3) Scenario 3: load levels of 200, 315, and 430 MW are selected with an IM penetration rate of 30%. According to (15)-(19), an increase in load level enhances the frequency regulation effects of loads in terms of voltage dynamics, frequency dynamics, and inertia contribution. Meanwhile, the sensitivity $k_{sens,ik}$ of load voltage magnitude to active power variation also varies under different load levels due to differences in the Jacobian matrix elements. Table VI presents the calculation results of the relevant parameters under different load levels.

TABLE VI
CALCULATION RESULTS OF RELEVANT PARAMETERS UNDER DIFFERENT LOAD LEVELS

Parameter	Value		
	200 MW	315 MW	430 MW
$k_{sens,58}$	–0.0140	–0.0276	–0.0534
$k_{sens,68}$	–0.0158	–0.0284	–0.0586
$k_{sens,88}$	–0.0435	–0.0567	–0.1272
K_{IM}	1.21	1.94	2.67
H_L (s)	0.456	0.741	1.180
T_{IM} (s)	0.0621	0.0673	0.0700
R_{IM}	0.8972	0.9290	0.9490
F_{IM}	27.94	26.67	25.80

The comparison of frequency responses of the proposed model and Model 1 and the maximum frequency error of proposed model under different load levels are shown in Fig. 11. Figure 11 shows that the proposed model has relatively small errors and can reflect the SFR under different load levels. Meanwhile, the system frequency drop slows down as the load level increases. Specifically, the RoCoF, the maxi-

mum frequency deviation $\Delta\omega_{max}$, and quasi-steady-state frequency deviation $\Delta\omega_{qss}$ gradually decrease with increasing load level. The primary reason for this influence pattern is that an increase in load level enhances the load voltage dynamics ($k_{sens,ik}$) and inertia contribution (H_L). Specifically, the increase of the load level enlarges $k_{sens,ik}$. The active power variations caused by load voltage dynamics are 1.54 MW, 2.59 MW, and 5.2 MW, accounting for 10%, 17.3%, and 34.7% of the frequency regulation share, respectively. These results demonstrate that the frequency regulation contribution from load voltage dynamics increases proportionally with the load level, a conclusion that is strongly supported by $\Delta\omega_{qss}$ under varying load levels. Additionally, the load inertia increases from 0.456 s to 1.18 s, accounting for 28.3% of the total system inertia. This results in reductions of $RoCoF_{max}$ and $\Delta\omega_{max}$.

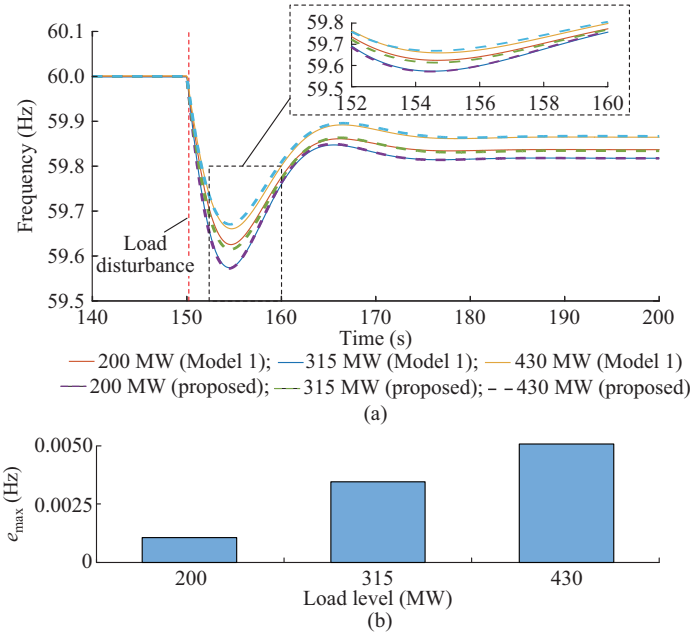

Fig. 11. Comparison of frequency responses of proposed model and Model 1 and the maximum frequency error of proposed model under different load levels. (a) Comparison of frequency responses. (b) The maximum frequency error of proposed model.

C. Effect of Load Parameters on Frequency Stability Indicators

From the above analysis, it can be concluded that the accuracy of the proposed model is sufficient to characterize the SFR under various load dynamics. To further explore the impact of load parameters on frequency stability indicators, the effects of IM penetration rate, IM rotor inertia, and load level on $RoCoF_{max}$, $\Delta\omega_{max}$, and $\Delta\omega_{qss}$ are investigated. The relevant results are shown in Fig. 12.

As shown in Fig. 12(a), the increase of the IM rotor inertia, load level, and IM penetration rate results in the decrease of $RoCoF_{max}$, with IM rotor inertia having the greatest impact. In large power grids, IM penetration rates typically range from 40% to 60% and IM rotor inertia typically ranges from 3 to 5 s, resulting in $RoCoF_{max}$ being less than 0.14 Hz/s. In this context, as load levels increase, $RoCoF_{max}$ decreases, with a minimum of 0.08 Hz/s. This indicates that increased load levels alter the effective inertia provided by the load (H_L) to the system. Additionally, higher load levels lower the voltage magnitude at load buses, thereby diminishing the impact of load voltage dynamics. These two factors together explain the relatively minor impact of load levels on $RoCoF_{max}$.

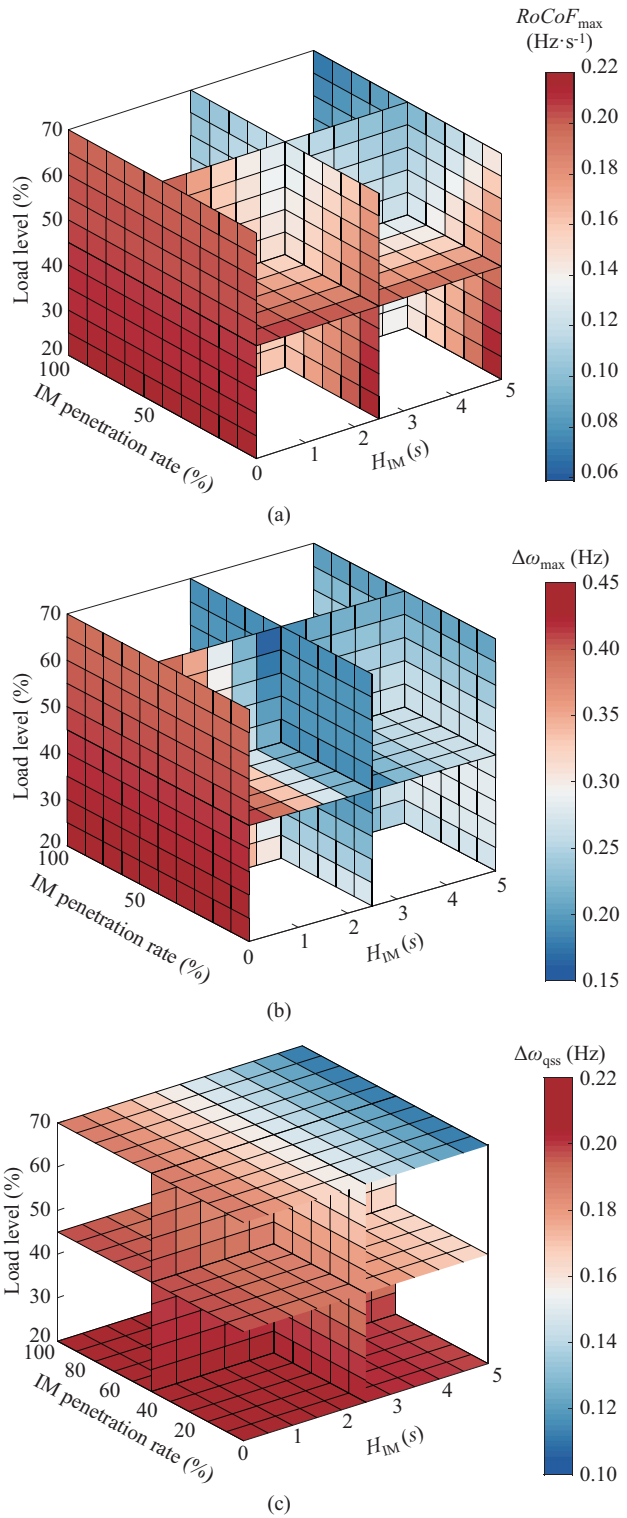

Fig. 12. Effect of load parameters on frequency stability indicators. (a) Effect of load parameters on $RoCoF_{max}$. (b) Effect of load parameters on $\Delta\omega_{max}$. (c) Effect of load parameters on $\Delta\omega_{qss}$.

As shown in Fig. 12(b), the IM penetration rate has almost no impact on $\Delta\omega_{max}$ because the IM penetration rate has minimal effect on load inertia (H_L) and primary frequency regulation gain of loads ($1/R_{IM}$). By contrast, IM rotor inertia and load level significantly influence $\Delta\omega_{max}$. If the actual power grid operates at a medium load level, $\Delta\omega_{max}$ does not exceed 0.35 Hz, which is the result of the combined effects of load voltage dynamics, load frequency dynamics, and inertia contributions.

As shown in Fig. 12(c), the IM penetration rate has the least impact on $\Delta\omega_{qss}$, the IM rotor inertia has a moderate impact, and the load level has the greatest impact. This is primarily because $\Delta\omega_{qss}$ is inversely proportional to the primary frequency regulation gain of the system ($1/R_e$). The load level directly alters the extent of IM participation in the system primary frequency regulation. In a medium load level grid, $\Delta\omega_{qss}$ is less than 0.16 Hz. Additionally, as load levels increase, the impact of load voltage dynamics on $\Delta\omega_{qss}$ becomes more significant. These two factors together reveal the influence of load level on the system primary frequency regulation and $\Delta\omega_{qss}$.

The above impacts of loads on system frequency stability indicators clearly demonstrate that IM rotor inertia, IM penetration rate, and load levels all contribute to the system inertia, affecting the initial frequency response to disturbances. The load level significantly influences the primary frequency regulation of the system. This implies that heavy load levels play an important role in mitigating frequency variations in the system.

VI. Conclusion

This paper presents an aggregated SFR model considering load dynamics. The proposed model is validated using the WECC 9-bus test system, which includes power electronic sources. The proposed model is compared with the time-domain simulation model and the traditional SFR model, and the impact of load parameters on system frequency is further analyzed. The variety of the conditions analyzed is representative of many conditions that can also be found in larger power systems.

The main conclusions are as follows.

1) Through small-signal modeling, load dynamics are categorized into three components: voltage-active power dynamics, frequency-active power dynamics, and inertia contributions. It is observed that the proposed model accurately captures the impact of different load types on system frequency across various scenarios.

2) The proposed model aggregates different load types within the system. Under different conditions of IM penetration rate, IM rotor inertia, and load level, the maximum error in the system frequency response is less than 0.006 Hz, demonstrating the high accuracy of the model.

3) The analysis of the impact of load parameters on frequency stability indicators reveals that the IM rotor inertia and load levels are critical factors in mitigating system frequency variations.

Future work will adopt the proposed model to further investigate the specific aspects of the load dynamics in bulk power systems. In particular, the three parts identified for representing the load dynamics will be considered in the interactions with different types of generators with specific frequency regulation capabilities.

Appendix A

The numerical positive and negative properties of (11) are equivalent:

$$\begin{cases} m_{\omega_s} = 1 - 2\dfrac{R_{sr}\left(R_s + R_r/s_{slip0}\right) + x_{sr}^2}{\left(R_s + R_r/s_{slip0}\right)^2 + x_{sr}^2} \\ m_{\omega_r} = -\left[1 - 2\dfrac{R_s\left(R_s + R_r/s_{slip0}\right) + x_{sr}^2}{\left(R_s + R_r/s_{slip0}\right)^2 + x_{sr}^2}\right] \end{cases} \tag{A1}$$

where m_{ω_s} and m_{ω_r} are the coefficients of K_{T_e,ω_e} and K_{T_e,ω_r}, respectively.

Clearly, $m_{\omega_s} \approx -m_{\omega_r}$. For the high-power IM, the initial slip ratio $s_{slip0} < 1\%$, which then satisfies:

$$R_s + R_r/s_{slip0} >> x_{sr} \tag{A2}$$

So that (A1) is simplified to:

$$m_{\omega_s} \approx 1 - 2\frac{R_{sr}}{R_s + R_r/s_{slip0}} \tag{A3}$$

The short-circuit resistance is much less than the load-equivalent resistance during normal operation of the IM, so $R_{sr}/\left(R_s + R_r/s_{slip0}\right) < 0.5$, and a generalized conclusion exists:

$$\begin{cases} m_{\omega_s} > 0 \\ m_{\omega_r} < 0 \end{cases} \tag{A4}$$

References

[1] N. Hatziargyriou, J. Milanovic, C. Rahmann *et al.*, "Definition and classification of power system stability – revisited & extended," *IEEE Transactions on Power Systems*, vol. 36, no. 4, pp. 3271-3281, Jul. 2021.

[2] M. Farrokhabadi, C. A. Canizares, J. W. Simpson-Porco *et al.*, "Microgrid stability definitions, analysis, and examples," *IEEE Transactions on Power Systems*, vol. 35, no. 1, pp. 13-29, Jan. 2020.

[3] A. Tayyebi, D. Gross, A. Anta *et al.*, "Frequency stability of synchronous machines and grid-forming power converters," *IEEE Journal of Emerging and Selected Topics in Power Electronics*, vol. 8, no. 2, pp. 1004-1018, Jun. 2020.

[4] J. Meng, Y. Mu, J. Wu *et al.*, "Dynamic frequency response from electric vehicles in the Great Britain power system," *Journal of Modern Power Systems and Clean Energy*, vol. 3, no. 2, pp. 203-211, Mar. 2015.

[5] C. Wang, Z. Wang, J. Wang *et al.*, "Robust time-varying parameter identification for composite load modeling," *IEEE Transactions on Smart Grid*, vol. 10, no. 1, pp. 967-979, Jan. 2019.

[6] Y. Bian, H. Wyman-Pain, F. Li *et al.*, "Demand side contributions for system inertia in the GB power system," *IEEE Transactions on Power Systems*, vol. 33, no. 4, pp. 3521-3530, Jul. 2018.

[7] P. M. Anderson and M. Mirheydar, "A low-order system frequency response model," *IEEE Transactions on Power Systems*, vol. 5, no. 3, pp. 720-729, Aug. 1990

[8] Q. Shi, F. Li, and H. Cui, "Analytical method to aggregate multi-machine SFR model with applications in power system dynamic studies," *IEEE Transactions on Power Systems*, vol. 33, no. 6, pp. 6355-6367, Nov. 2018.

[9] K. Yan, G. Li, R. Zhang *et al.*, "Aggregated SFR model for VSC-HVDC interconnected power systems with high penetration of wind power," *Electric Power Systems Research*, vol. 216, p. 109018, Mar. 2023.

[10] M. Garmroodi, D. J. Hill, G. Verbic *et al*., "Impact of load dynamics on electromechanical oscillations of power systems," *IEEE Transactions on Power Systems*, vol. 33, no. 6, pp. 6611-6620, Nov. 2018.
[11] A. Adrees and J. Milanović, "Effect of load models on angular and frequency stability of low inertia power networks," *IET Generation, Transmission & Distribution*, vol. 13, no. 9, pp. 1520-1526, May 2019.
[12] C. Concordia and S. Ihara, "Load representation in power system stability studies," *IEEE Transactions on Power Apparatus and Systems*, vol. PAS-101, no. 4, pp. 969-977, Apr. 1982.
[13] G. Delille, J. Yuan, and L. Capely, "Taking advantage of load voltage sensitivity to stabilize power system frequency," in *Proceedings of 2013 IEEE Grenoble Conference*, Grenoble, France, Jun. 2013, pp. 1-6.
[14] S. Liao, J. Xu, Y. Sun *et al*., "Load-damping characteristic control method in an isolated power system with industrial voltage-sensitive load," *IEEE Transactions on Power Systems*, vol. 31, no. 2, pp. 1118-1128, Mar. 2016.
[15] H. Huang and F. Li, "Sensitivity analysis of load-damping characteristic in power system frequency regulation," *IEEE Transactions on Power Systems*, vol. 28, no. 2, pp. 1324-1335, May 2013.
[16] L. Sigrist and L. Rouco, "An induction motor model for system frequency response models," *International Transactions on Electrical Energy Systems*, vol. 27, no. 11, p. e2413, Nov. 2017.
[17] L. Chen, X. Wang, Y. Min *et al*., "Modelling and investigating the impact of asynchronous inertia of induction motor on power system frequency response," *International Journal of Electrical Power & Energy Systems*, vol. 117, p. 105708, May 2020.
[18] P. Tielens and D. van Hertem, "The relevance of inertia in power systems," *Renewable and Sustainable Energy Reviews*, vol. 55, pp. 999-1009, Mar. 2016.
[19] D. P. Chassin, Z. Huang, M. K. Donnelly *et al*., "Estimation of WECC system inertia using observed frequency transients," *IEEE Transactions on Power Systems*, vol. 20, no. 2, pp. 1190-1192, May 2005.
[20] M. R. B. Tavakoli, M. Power, L. Ruttledge *et al*., "Load inertia estimation using white and grey-box estimators for power systems with high wind penetration," *IFAC Proceedings Volumes*, vol. 45, no. 21, pp. 399-404, Sept. 2012.
[21] H. Thiesen and C. Jauch, "Determining the load inertia contribution from different power consumer groups," *Energies*, vol. 13, no. 7, p. 1588, Apr. 2020.
[22] Z. Ma, Z. Wang, Y. Wang *et al*., "Mathematical representation of WECC composite load model," *Journal of Modern Power Systems and Clean Energy*, vol. 8, no. 5, pp. 1015-1023, Sept. 2020
[23] Y. Lin and J. Wang, "A generic dynamic load model framework," *Journal of Modern Power Systems and Clean Energy*, vol. 10, no. 2, pp. 399-406, Mar. 2022
[24] H. Renmu, M. Jin, and D. J. Hill, "Composite load modeling via measurement approach," *IEEE Transactions on Power Systems*, vol. 21, no. 2, pp. 663-672, May 2006.
[25] J. V. Milanovic, K. Yamashita, S. M. Villanueva *et al*., "International industry practice on power system load modeling," *IEEE Transactions on Power Systems*, vol. 28, no. 3, pp. 3038-3046, Aug. 2013.
[26] L. Chavarro-Barrera, S. Perez-Londono, and J. Mora-Florez, "An adaptive approach for dynamic load modeling in microgrids," *IEEE Transactions on Smart Grid*, vol. 12, no. 4, pp. 2834-2843, Jul. 2021.
[27] X. Zhang, C. Zhao, J. Ma *et al*., "Optimized auxiliary frequency control of wind farm based on piecewise reduced-order frequency response model," *Journal of Modern Power Systems and Clean Energy*, vol. 12, no. 3, pp. 791-802, May 2024.
[28] C. Han, L. Shang, S. Su *et al*., "Grid synchronization control for grid-connected voltage source converters based on voltage dynamics of DC-link capacitor," *Journal of Modern Power Systems and Clean Energy*, vol. 12, no. 5, pp. 1678-1689, Sept. 2024.
[29] J. Ying, X. Yuan, J. Hu *et al*., "Impact of inertia control of DFIG-based WT on electromechanical oscillation damping of SG," *IEEE Transactions on Power Systems*, vol. 33, no. 3, pp. 3450-3459, May 2018.
[30] C. Li, Y. Yang, N. Mijatovic *et al*., "Frequency stability assessment of grid-forming VSG in framework of MPME with feedforward decoupling control strategy," *IEEE Transactions on Industrial Electronics*, vol. 69, no. 7, pp. 6903-6913, Jul. 2022.
[31] K. Yan, G. Li, R. Zhang *et al*., "Frequency control and optimal operation of low-inertia power systems with HVDC and renewable energy: a review," *IEEE Transactions on Power Systems*, vol. 39, no. 2, pp. 4279-4295, Mar. 2024.
[32] X. Liang and O. Ilochonwu, "Induction motor starting in practical industrial applications," *IEEE Transactions on Industry Applications*, vol. 47, no. 1, pp. 271-280, Jan. 2011.
[33] H. Jain, B. Mather, A. K. Jain *et al*., "Grid-supportive loads: a new approach to increasing renewable energy in power systems," *IEEE Transactions on Smart Grid*, vol. 13, no. 4, pp. 2959-2972, Jul. 2022.

Xianchao Liu received the B.S. and M.S. degrees in electrical engineering from Northeast Electric Power University, Jilin, China, in 2017 and 2020, respectively, where he is currently working toward the Ph.D. degree since Sept. 2020. From 2023 to 2024, he was a visiting Ph.D. student with the Department of Energy, Polytechnic University of Turin, Turin, Italy. His research interests include power system security and stability.

Guoqing Li received the B.S. and M.S. degrees in electrical engineering from Northeast Electric Power University, Jilin, China, in 1984 and 1988, respectively, and the Ph.D. degree in electrical engineering from Tianjin University, Tianjin, China, in 1998. He is currently a Professor with the Department of Electrical Engineering, Northeast Electric Power University, Jilin, China. His research interests include power system security and stability analysis, power system protection and optimization, and high-voltage direct current (HVDC).

Tao Huang received the Ph.D. degree from Polytechnic University of Turin, Turin, Italy, in 2011. He is currently an Associate Professor with the Department of Energy, Polytechnic University of Turin. He is also an Adjunct Professor with Xihua University, Chengdu, China, and Polytechnic University of Henan, Jiaozuo, China. His research interests include vulnerability assessment, electricity market, smart grid, active distribution network, and artificial intelligence in power system.

Tao Jiang received the B.S. and M.S. degrees in electrical engineering from Northeast Electric Power University, Jilin, China, in 2006 and 2011, respectively, and the Ph.D. degree in electrical engineering from Tianjin University, Tianjin, China, in 2015. He is currently a Professor with the Department of Electrical Engineering, Northeast Electric Power University. From 2014 to 2015, he was a Visiting Scholar with the Department of Electrical and Computer Engineering, North Carolina State University, Raleigh, USA. From Oct. 2018 to Oct. 2019, he was a Visiting Scholar with the Department of Electrical Engineering and Computer Science, University of Tennessee, Knoxville, USA. His research interests include power system stability analysis and control, renewable energy integration, and integrated energy system.

Soheil Saadatmandi received the B.Sc. degree in electronic engineering from Bahonar University of Kerman, Kerman, Iran, in 2014, and the M.Sc. degree in electrical engineering from Polytechnic University of Milan, Milan, Italy, in 2018. He was a Research Assistant at the University of Bergamo, Bergamo, Italy, from 2019 to 2020. He is currently a Ph.D. student at Polytechnic University of Turin, Turin, Italy. His research interests include power system analysis, smart grid, microgrid, electric vehicle smart charging, and renewable energy technology.

Gianfranco Chicco is a Full Professor of electrical energy systems with Polytechnic University of Turin, Turin, Italy. He was the 2023-2024 Chair of the IEEE R8 Italy Section. He is the Editor-in-Chief of Sustainable Energy Grids and Networks. He was the Conference Chair of WESC 2006, IEEE PES ISGT Europe 2017, UPEC 2020, IEEE Eurocon 2023, and SEST 2024, and a Co-chair of IEEE SmartGridComm 2024. He is a member of the Italian Association AEIT. His research interests include power system analysis, distribution system analysis and optimization, electrical load management, energy efficiency and environmental impact of multi-energy systems, data analytics applied to power and energy systems, and power quality.